Novel Red-Emitting Copper(I) Complexes with Pyrazine and Pyrimidinyl Ancillary Ligands for White Light-Emitting Electrochemical Cells

Elisa Fresta, Gilbert Mahoro, Luca Cavinato, Jean-francois Lohier, Jean-luc Renaud, Sylvain Gaillard, Rubén Costa

ADVANCED OPTICAL MATERIALS
www.advopticalmat.de

Novel Red-Emitting Copper(I) Complexes with Pyrazine and Pyrimidinyl Ancillary Ligands for White Light-Emitting Electrochemical Cells

Elisa Fresta, Gilbert U. Mahoro, Luca M. Cavinato, Jean-Francois Lohier, Jean-Luc Renaud, Sylvain Gaillard, and Rubén D. Costa**

The synthesis, photophysical/electrochemical characterization, and implementation in light-emitting electrochemical cells (LECs) of three novel red-emitting heteroleptic [Cu(N^N)(P^P)]PF_6 complexes are reported. The complex design consists in combining i) the bridged di(pyrazin-2-yl)sulfane N^N ligand with expanded π-conjugation and electro-withdrawing 4-(trifluoromethyl) pyrimidine moieties and ii) the [(diphenylphosphino)phenyl] ether (DPEphos) P^P ligand. The effect of the N^N ligand substitution on the photophysical, electrochemical, ion conductivity, and morphological features in their respective powders and thin films is thoughtfully rationalized. This is rounded by the trends noted in single-layered red-emitting LECs (λ_{max} = 630–660 nm) featuring moderate performances with irradiances of around 60–90 µW cm^{-2} and total emitted energies in the range of 4–12 mJ. A further optimization using a multilayered architecture, in which hole injection/transport and exciton formation processes are decoupled, leads to a significant enhancement of the irradiance up to ≈150 µW cm^{-2} and total emitted energies of 91 mJ without affecting device chromaticity. Finally, the best red-emitting complex in LECs is used to fabricate host:guest white devices, achieving luminances of 12 cd m^{-2} in concert with an excellent white color quality (*x*/*y* CIE color coordinates of 0.31/0.32; color rendering index of 90) stable over lifespan.

1. Introduction

The quest for efficient, low-cost, and sustainable lighting technologies remains crucial. Over the last two decades, the electroluminescence process in solid-state lighting (SSL) has established itself as the future of the artificial lighting.[1,2] Among the SSL concepts, light-emitting electrochemical cells (LECs) are of high interest due to i) their simple architecture, ii) the low-cost and up-scalable fabrication process, and iii) the possibility of achieving sustainable, all solution-based processed devices for moderate performing lighting purposes.[3,4] In short, LECs consist of a thin-film made of an electroluminescent material that is either charged and/or doped with ionic electrolytes sandwiched between two air-stable electrodes.[5,6] The ionic species are randomly distributed across the active layer at zero bias, while they rearrange toward the oppositely charged electrodes forming electric double layers (EDLs) upon application of an external bias.[5] This allows efficient charge injection and the subsequent formation of p- and n-doped regions that are separated by a nondoped region, in which exciton recombination takes place.[5,7–9]

A wide variety of emitters has been applied to LECs, such as conjugated polymers, small molecules, and ionic transition metal complexes (iTMCs).[6,10–15] As far as the iTMCs are concerned, efforts have recently been put toward replacing traditional Ir(III) and Ru(II)-based iTMCs by Cu(I)-counterparts (Cu-iTMCs).[11,16,17] In particular, we[18–21] and others[22–26] have mainly explored LECs with heteroleptic $[Cu(P^P)(N^N)]^+$ complexes, achieving efficiencies of up to 5 cd A^{-1}, stabilities of a few hundred hours, and luminances of a couple of hundreds cd m^{-2}.[24–27] However, these devices are limited to the green- and yellow-emitting regions, while blue Cu-iTMC-LECs have been realized with the NHC-dipyridilamine Cu-iTMC family (NHC is *N*-heterocyclic carbene)[28] and a single work on red Cu-iTMC-LECs was recently reported in a series of heteroleptic $[Cu(P^P)(N^N)]^+$[20] with the 4,4′-diethylester-2,2′-biquinoline N^N ligand and different P^P ligands. Here, the best LECs featured λ_{max} = 673 nm, *x*/*y* CIE color coordinates of 0.66/0.32, and irradiances of ≈100 µW cm^{-2} at pulsed 15 mA.[29]

E. Fresta, L. M. Cavinato, R. D. Costa
Technical University of Munich
Chair of Biogenic Functional Materials
Schulgasse 22, 94315 Straubing, Germany
E-mail: ruben.costa@tum.de
G. U. Mahoro, J.-F. Lohier, J.-L. Renaud, S. Gaillard
LCMT-Caen
ENSICAEN, UNICAEN, CNRS
Normandie Univ
Caen 14000, France
E-mail: sylvain.gaillard@ensicaen.fr
G. U. Mahoro
Universidad Autónoma de Madrid
Departamento de Física Aplicada
Calle Francisco Tomás y Valiente, Madrid 28049, Spain
The ORCID identification number(s) for the author(s) of this article can be found under https://doi.org/10.1002/adom.202101999.

DOI: 10.1002/adom.202101999

Thus, further developments in designing low-energy emitting Cu-iTMCs for LECs are all instrumental to realize high-performing Cu-iTMC-based white-emitting LECs.[30,31] In this context, we have recently described the effect of the bridged atom in the bis-pyridyl N^N ligand using either NHC[32] or P^P[17] as counter main ligands toward rainbow Cu-iTMCs. Among them, a large red-shift in emission was realized with the py-S-py bridged N^N ligand ((dipyrid-2-yl)sulfane), but this came with the trade-off of thin films with very low photoluminescence quantum yields (PLQYs < 1%) and ionic conductivities (σ; $\approx 1 \times 10^{-9}$ S m^{-1}) that led to nonfunctional LECs.[17,33]

Herein, we redesign this family of complexes, realizing a series of highly emissive red-emitting Cu-iTMCs that led to best-performing red- and white-LECs up to date. In short, the py-S-py ligand was modified by i) changing the pyridine for pyrazine (i.e., di(pyrazin-2-yl)sulfane pz-S-pz N^N ligand in complex **1**; **Figure 1**), ii) introducing π-extended and electron-poor quinoxaline rings (i.e., 2-(pyrazin-2-ylthio)quinoxaline pq-S-pz in complex **2**; Figure 1), and iii) employing an electron-withdrawing substituent, i.e., a 4-trifluoromethylpyrimidine moiety (i.e., 2-(pyrazin-2-ylthio)-4-(trifluoromethyl)pyrimidine pz-S-(4-CF_3-pm) in complex **3**; Figure 1). This design led to a significant decrease of the highest occupied molecular orbital–lowest unoccupied molecular orbital (HOMO–LUMO) gap compared to previous complexes with py-S-py, moving the emission from the yellowish to the reddish region, while keeping high PLQYs in thin films. Indeed, the best LECs were realized with **1** featuring irradiances of 90 µW cm^{-2} along with total emitted energy (E_{tot}) of 12 mJ associated with a red emission centered at 630 nm and x/y CIE color coordinates of 0.59/0.41.[20] This was further optimized using a multilayered architecture (i.e., using 4,4′-bis(*N*-carbazolyl)-1,1′-biphenyl (CBP)-based hole transport thin film) to decouple hole injection/transport and exciton formation, realizing LECs with one order of magnitude improved figures-of-merit without affecting device chromaticity. Finally, this was exploited to fabricate host:guest white-emitting LECs, in which CBP and **1** were the host and guest, respectively. These devices exhibited luminances of 12 cd m^{-2} and an excellent white color quality (i.e., x/y CIE coordinates of 0.31/0.32 and CRI of 90) stable over their lifespan, representing the best-performing Cu-iTMC white LEC to date.[20,30,31] Overall, this work provides a rational design to prepare enhanced red-emitting Cu-iTMCs with bridged bis-pyrimidinyl ancillary ligands that led to the best-performing red- and white-emitting LECs up to date.

2. Results and Discussion

2.1. Synthesis of Complexes 1–3

Scheme 1 displays the synthesis procedure of compounds **1–3**. At first, the synthesis of thiopyrimidine **4** was prepared from the thiolation of the corresponding halides using NaHS·H_2O 90% and was obtained in 66% isolated yield (Scheme 1).[34] Then sulfide **5–7** were prepared via S_NAr reaction. In mild conditions, using K_2CO_3 as base and CH_3CN as solvent,[35] 2-thiopyrimidine **4** as nucleophile introduced with the appropriated electrophile, i.e., 2-iodopyrazine and 2-chloroquinoxaline as electrophile successfully furnished pz-S-pz **5** and pq-S-pz **6** with 59% and 80% isolated yield, respectively. For the synthesis of pz-S-(4-CF_3-pm) **7**, starting from **4** and 2-chloro-4-(trifluoromethyl)pyridine, the use of the stronger base, KOH in dimethyl sulfoxide (DMSO), at 140 °C was required to give the desired pz-S-(4-CF_3-pm) **7** in 64% isolated yield.[36] Next, complexes **1–3** were prepared following a standard procedure described in the literature.[37] The sulfide ligands were added to a mixture of $[Cu(MeCN)_4][PF_6]$ and DPEphos in stoichiometric conditions in dry and degassed CH_2Cl_2 under argon atmosphere. All products were purified by recrystallization furnishing pure complexes **1–3** in 91%, 91%, and 86% isolated yields, respectively. Complexes **1–3** were then characterized by ^{1}H, ^{13}C, ^{18}F, and ^{31}P NMR spectroscopy and high-resolution mass spectrometry—see Supporting Information for detailed procedure and characterization.

2.2. Structural Characterization

Suitable X-ray diffraction (XRD) quality single crystals were grown by slow gas diffusion of a mixture of pentane and ether into CH_2Cl_2 solutions of the compounds. Only **1** and **2** were able to produce suitable single crystals for structural analysis. The ellipsoid representations of **1** and **2** are shown in **Figure 2**, while the selected bond angles and lengths are gathered in Table S1 in the Supporting Information. The XRD data are reported in Table S2 in the Supporting Information. The compounds were crystallized in monoclinic space group $P2_1/c$ (14) for **1** and triclinic space group $P\bar{1}$(2) for **2**. The introduction of the quinoxaline moiety in compound **2** leads to a decrease of the P—Cu—P bite angle 110.39(3)° and N—Cu—N with 90.93(9)° compared to those of compound **1** with values of 116.64(3)° for P—Cu—P bite angle and 93.13(8)° for N—Cu—N. On the other

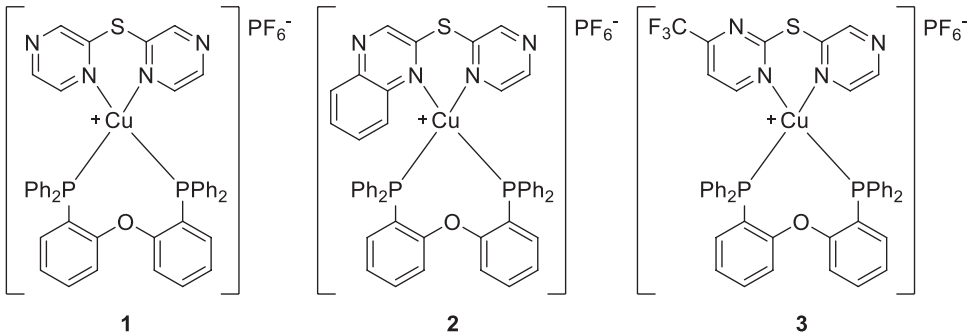

1 2 3

Figure 1. Chemical structures of complexes **1–3**.

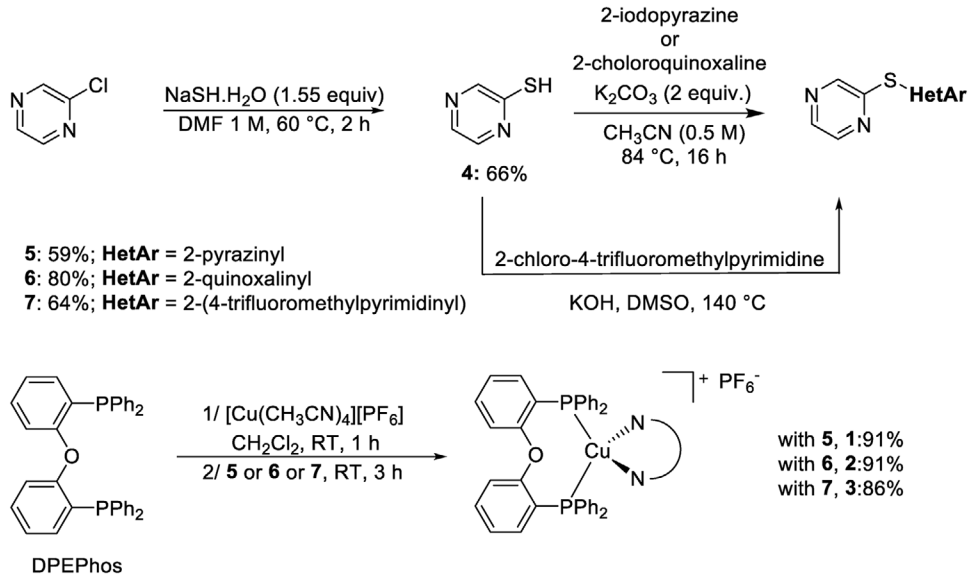

Scheme 1. Synthetic routes for the synthesis of complexes **1**–**3**.

hand, the Cu—P and Cu—N bond lengths are increased in **2**. The τ_4 geometrical index defined by Houser for tetracoordinate complexes[38] is 0.76 and 0.84 for **1** and **2**, respectively. Houser and co-workers defined a perfect tetrahedral geometry for a τ_4 of 1 and a perfect trigonal pyramidal geometry for a τ_4 of 0.85. Consequently, **1** and **2** possess more likely a trigonal pyramidal geometry.

2.3. Photophysical and Electrochemical Studies

The UV-vis absorption spectra of **1**–**3** were recorded in dichloromethane (DCM) solutions and thin films (**Table 1**; **Figure 3** and Figure S1, Supporting Information). Thin films (60–70 nm) were prepared on quartz via spin-coating using butanone solutions (see the Experimental Section for details). In both cases, they featured intense absorption bands in the range of 240–360 and 350–450 nm that are attributed to ligand-centered (LC) and metal-to-ligand charge transfer (MLCT) transitions, respectively.[20,33] The photoluminescence features of **1**–**3** were also investigated in DCM solution, powder, and thin film (Figure 3 and Table 1). All the complexes are not emissive in solution, as they are prone to easy conformational changes assisted by weak solvent interaction upon excitation. In contrast, intense, broad, and structureless emission bands centered at 580, 640, and 650 nm were noted for the crystalline powders of **1**, **2**, and **3**, respectively. As expected,[39,40] the emission is associated with average excited state lifetimes $<\tau>$ spanning from 6 to 10 µs at room temperature (Table 1 and Figure S2, Supporting Information). Much more relevant, the PLQYs were strongly enhanced compared to the reference compound with py-S-py ligand (i.e., <1%),[17,33] reaching values of ≈25% (**1**), 60% (**2**), and 8% (**3**). Upon close inspection of the X-ray structures, the enhanced PLQYs could be related to weak intra- and intermolecular interactions between ligands in the complexes. Indeed, it is now commonly accepted that rigid complex structure helps to obtain very bright emitters. Consequently, the presence of weak interactions, giving a more rigid structure, should reduce vibrational loss of energy. Similar to copper(I) complexes bearing py-S-py and DPEphos ligands (Tables S3 and S4, Supporting

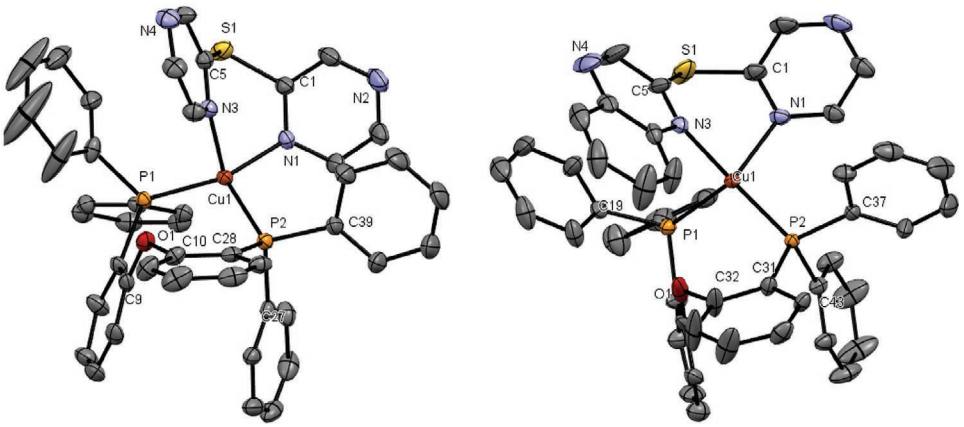

Figure 2. Ellipsoid representations of **1** (left) and **2** (right) at 50% probability.

Table 1. Photophysical properties of **1–3** in solution and thin films.

Complex	Absorption		Emission			PLQY		<τ>		
	λ_{max} [a] [nm]	λ_{max} [b] [nm]	λ_{max} [b),c)] [nm]	λ_{max} [d),e)] [nm]	λ_{max} (77 K) [b),c)] [nm]	[%] [b),c)]	[%] [d),e)]	[µs] [b),c)]	[µs] [d),e)]	(77 K) [µs] [b),c)]
1	249, 275, 325, 369	268, 293, 400	634	581	645	7.1	23.7	1.4	10.5	11.6
2	242, 267, 291, 353, 428	271, 289, 363, 428	661	642	675	4.9	57.8	0.90	6.47	2.4
3	248, 285, 321, 369	251, 271, 289, 415	653	650	671	3.1	7.7	1.07	7.71	2.1

[a]DCM solution; [b]Thin films; [c]λ_{exc} = 330 nm; [d]Crystalline powder; [e]λ_{exc} = 355 nm.

Information),[17,33] **1** and **2** exhibit different weak interactions, such as O···H interaction between the oxygen atom of the DPEphos ligand and one hydrogen atom of the N^N ligand, CH–π interaction between an aromatic ring with an hydrogen atom of another aromatic ring, and π–π interactions between two aromatic rings (Tables S5–S8, Supporting Information). In detail, one O···H and one π–π interactions were noted in the XRD structure of **1**, while the π–π interaction is stronger than that in the previous complex having py-S-py ligand (i.e., centroid distances of 3.6386(2) and 3.720(3) Å for **1** and complex bearing py-S-Py; Tables S3 and S5, Supporting Information). Importantly, **2** showed three π–π and three CH–π interactions that lead to the most rigid structure in this series (Tables S7 and S8, Supporting Information). Hence, a trend of rigidity is complex having py-S-py < **1** < **2** going hand-in-hand with that of the PLQYs, i.e., <1% < 23.7% < 57.8%, respectively.

In stark contrast, thin films showed a red-shifted broad emission band (Figure 3). This is typically ascribed to a short- and/or large-range aggregation tendency.[41] Indeed, the presence of aromatic moieties favors the formation of π–π stacking interactions and aggregation features in amorphous solid state. Atomic force microscopy (AFM) images showed films with neither apparent phase separation nor large aggregates, a root mean square roughness between <5 nm, and small (<10 nm) hillocks formations that might be related to the slow evaporation of butanone upon film forming (Figure S3, Supporting Information). Thus, the films are suitable for device fabrication. However, a short-range aggregation that may lead to charge trapping phenomena and/or emission quenchers must be present as indicated by the reduction of both, <τ> and PLQY values, compared to those in powder (Table 1).

This prompted us to evaluate the temperature-dependence behavior of the photoluminescence in thin films. In short, changes in emission band shape and <τ> were monitored in inert atmosphere upon increasing the temperature from 77 to 360 K (**Figure 4** and Figure S4, Supporting Information). At first, the maximum wavelength of the emission band gradually blue-shifts upon increasing the temperature. This is a qualitative indication of a thermally activated delayed fluorescence (TADF) mechanism in Cu-iTMCs.[42] Commonly, TADF emitters are characterized by a small singlet-triplet energy separation (ΔE_{ST}) of ≈1000 cm^{-1} or 0.12 eV and a fast intersystem crossing (ISC), allowing the repopulation of the higher-lying S_1 states from the lower-lying T_1 states under suitable temperature conditions. This is investigated plotting τ versus T and fitting the tendency with Equation (1) as proposed by Kirchhoff et al. for heteroleptic $[Cu(P^P)(N^N)]^+$, where τ_{em} is the emissive average excited state lifetime at a certain T, K_b represents the Boltzmann constant (1.38×10^{-23} m^2 kg s^{-2} K^{-1}) and $\tau(T_1)$ and $\tau(S_1)$ are the long and short components of the excited state lifetime, respectively[43,44]

$$\tau_{em}(T) = \frac{3 + \exp\left(-\frac{\Delta E(S_1 - T_1)}{k_B \cdot T}\right)}{\frac{3}{\tau(T_1)} + \frac{1}{\tau(S_1)} \times \exp\left(-\frac{\Delta E(S_1 - T_1)}{k_B \cdot T}\right)} \quad (1)$$

In this series, the fit led to ΔE_{ST} values spanning from 0.06 to 0.13 eV (Figure 4 and Figure S4, Supporting Information).

Assuming that the PLQY does not depend on the temperature and the population of the two states (S_1 and T_1) adheres to

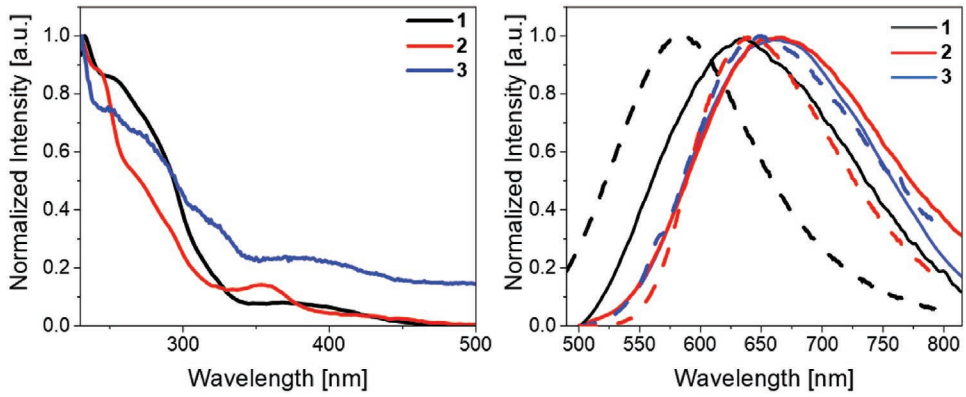

Figure 3. UV-vis absorption spectra (left) of **1–3** in DCM (5×10^{-5} M) and emission spectra (right) of **1–3** in thin films (solid line) and powder (dashed line).

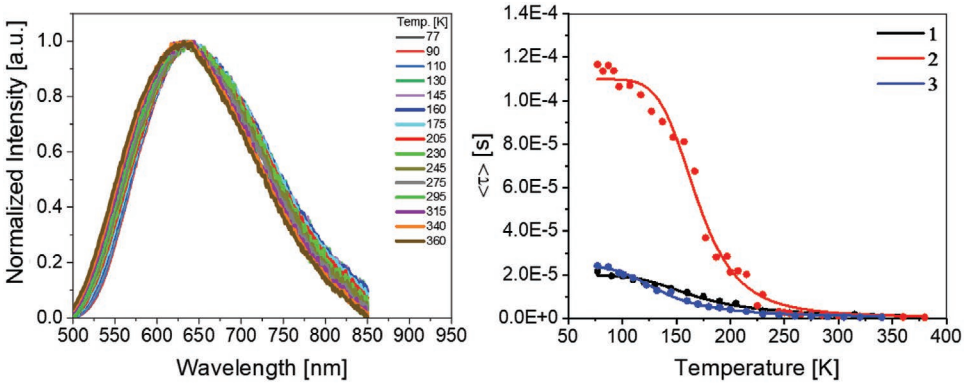

Figure 4. Emission spectra in the range of 77–360 K (see legend) of **1** thin films (left) and τ_{em} of **1–3** in thin film in the temperature range of 77–400 K fitted with Equation (1) (right). The fitting is shown in solid lines.

the Boltzmann distribution, it is possible to estimate the individual proportions of the two photoluminescence processes at a defined temperature following Equation (2). $I(S_1)$ denotes the TADF intensity originating from the S_1 state and $I(T_1)$ the phosphorescence intensity from the T_1 state

$$\frac{I(S_1)}{I(T_1)} = \frac{k_r(S_1)}{3k_r(T_1)} \times \exp\left(-\frac{\Delta E(S_1 - T_1)}{k_B \cdot T}\right) \quad (2)$$

where k_r is the radiative constant of the singlet (S1) or triplet (T1) state.

At 300 K, the TADF comprises 94% of the total emission for **1** and **3**, inferring an efficient reverse ISC, while **2** exhibits a 76% TADF process responsible for the emission. Interestingly, **3** has a low PLQY in thin film (Table 3), highlighting that an efficient TADF process does not directly imply high PLQYs, since parasitic nonradiative pathways may also be thermally activated.[45] Indeed, the high PLQYs in a TADF materials is reached both with a suitable HOMO–LUMO spatial separation to give a small ΔE_{ST} and allow for successful reverse ISC, and an efficient exciton deactivation to convert all generated singlet excitons into light emission through efficient singlet radiative transition.[45,46]

Finally, the electrochemical properties of **1–3** were studied using cyclic voltammetry (CV) in solution of DCM with 0.1 M n-Bu_4NPF_6 at room temperature (see the Experimental Section for details). They showed two irreversible oxidation peaks located at 0.70/1.04, 0.64/0.95, and 0.84/1.14 V for **1**, **2**, and **3**, respectively (**Figure 5** and **Table 2**). The first oxidation process is ascribed to the metal-centered oxidation that forms copper(II) species,[47,48] while the second one corresponds to the oxidation of the P^P ligand.[24] The presence of irreversible redox processes indicates that stability issues might rise in devices. In stark contrast, a quasi-reversible reduction process attributed to the N^N ligands is located around –1.65, –1.70, and –1.75 V for **1**, **2**, and **3**, respectively (Figure 5 and Table 2).[48]

2.4. Fabrication of Red- and White-Emitting LECs

1–3-based LECs were fabricated by first spin-coating a 70 nm layer of poly(3,4-ethylenedioxythiophene):polystyrene sulfonate (PEDOT:PSS) onto an indium tin oxide (ITO) electrode coated glass, followed by an active layer consisting of pristine **1–3** and the final 90 nm of aluminum cathode deposited via physical vapor deposition (see the Experimental Section for details). At first, consecutive irradiance–current–voltage scans were performed (Figure S5, Supporting Information). In the first scan, **1**-, **2**-, and **3**-based devices reached irradiances of ≈200, 55, and 85 µW cm^{-2} at 15 V, respectively. However, both, irradiance and applied current, significantly dropped upon increasing the number of scans reaching, e.g., values of <10 µW cm^{-2} at the third scan. This is in line with the electrochemical features of the Cu-iTMCs—vide supra, in which the irreversible formation of Cu(II) species has been noted as critical in terms of emission quenching and charge trapping.[18,19] This issue will be successfully addressed using multilayered LECs—vide infra.

Next, we performed static electrochemical impedance spectroscopy (EIS) measurements at different applied voltages ranging from 0 to 5 V and frequencies going from 1 to 1 × 10^6 Hz (see the Experimental Section for details).[20,50] EIS analyses of the Nyquist plots (Figure S6, Supporting Information) were conducted based on the equivalent circuit models shown in Figure S7 in the Supporting Information. **1**- and **3**-based

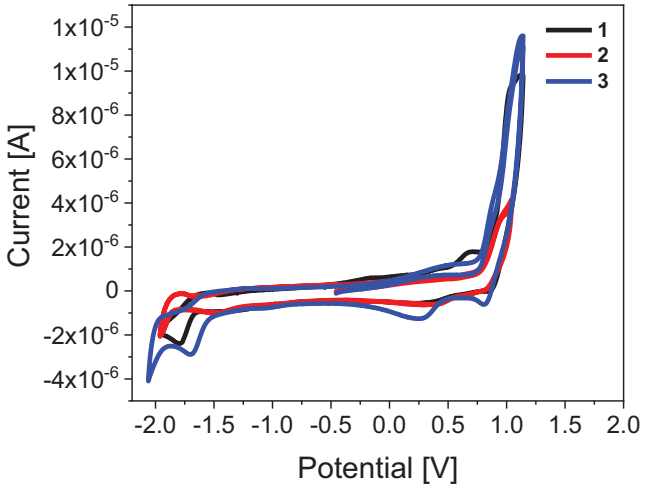

Figure 5. Cyclic voltammograms of **1–3** in DCM solution.

Table 2. Electrochemical features of **1–3** in solution and EIS parameters of **1–3** thin films.

Complex	Electrochemistry					EIS			
	E_{ox} [V]	E_{red} [V]	E_{HOMO}[a)] [eV]	E_{LUMO}[a)] [eV]	ΔE [eV]	R_{LEC} [Ω]	σ [S m^{-1}]	C_{eff} [nF]	ε
1	0.70, 1.04	−1.65	−5.6	−3.14	2.55	$3.4 \times 10^4 \pm 3.2 \times 10^3$	$2.2 \times 10^{-7} \pm 2.3 \times 10^{-6}$	9.9 ± 0.5	8.4 ± 0.9
2	0.64, 0.95	−1.75	−5.5	−3.08	2.47	$9.4 \times 10^5 \pm 9.1 \times 10^4$	$8.6 \times 10^{-9} \pm 9 \times 10^{-8}$	4.34 ± 0.6	3.9 ± 0.6
3	0.84, 1.14	−1.69	−5.6	−3.10	2.59	$1.4 \times 10^4 \pm 1.1 \times 10^3$	$5.7 \times 10^{-7} \pm 6.2 \times 10^{-6}$	9.26 ± 1.0	8.4 ± 1.2

[a)]Obtained from $E_{HOMO} = -(E[\text{onset}_{ox} \text{ vs } Fc^+/Fc] + 5.1 \text{ eV}$; $E_{LUMO} = -(E[\text{onset}_{red} \text{ vs } Fc^+/Fc] + 5.1 \text{ eV}$.[49]

devices showed the typical LEC resistance profile: i) an initial exponential decrease at biases below the energy gap of the emitter (<2 V) that corresponds to the formation of EDLs at the electrode interface and ii) a plateau that corresponds to the formation of the doped regions and the auto-sustained growth of the doped regions and charge recombination at the intrinsic region (**Figure 6**). In contrast, **2**-based devices showed two orders of magnitude higher resistance with a less pronounced reduction at high applied bias. This is in line with i) the higher turn-on voltages and lower driving currents exhibited by **2**-devices in the irradiance–current–voltage assays (Figure S5, Supporting Information) as well as ii) the calculations at 0 V of the dielectric constant (ε) of ≈8 and 3 as well as the σ of ≈10^{-7} and 10^{-8} S m^{-1} for **1**/**3**- and **2**-based devices, respectively (Table 2). Thus, lower stabilities and efficiencies are expected as **2**-devices will require high applied voltages to hold the current compliance in pulsed current driving schemes—vide infra. Interestingly, **2** also shows a dielectric constant ε of 3.4, which is less than half the value (8.4) obtained for **1** and **3** (Table 2). This implies a reduced polarizability of the layer that might be caused by the increased rigidity of the complex in the surrounding created upon film forming as well as the overall film morphology.

The devices were compared at 5 mA pulsed current (1 kHz, 50% duty cycle, on a 10 mm^2 pixel) monitoring the voltage and the electroluminescence intensity over time (**Table 3**; **Figure 7** and Figure S8, Supporting Information). In line with the photoluminescence in thin films, all the devices showed a red electroluminescence response consisting a broad and structureless band centered at ≈630, 660, and 625 nm for **1**, **2**, and **3** LECs, respectively. They are associated with x/y CIE color coordinates of 0.59–0.66/0.31–0.41 that hold over the entire measurement timespan in the red region (Figure S9 in the Supporting Information and Table 3). The maximum irradiance reached ≈90, 55, and 70 µW cm^{-2} associated with external quantum efficiencies (EQEs) of 0.032%, 0.016%, and 0.021% for **1**, **2**, and **3** LECs, respectively. These values are in line with the PLQYs in thin films and the EIS parameters—vide supra. In addition, they are in the range of the prior-art red LECs with, e.g., small molecules[51,52] and conjugated polymers.[53] Likewise, the device stability (Table 3) in terms of lifetimes ($t_{1/2}$, time to reach half of the maximum irradiance) or total emitted energy (E_{tot}, integrated radiant flux area from $t = 0$ to $t = 1/5$ of the maximum irradiance) are comparable to those reported for pristine Cu-iTMC-LECs,[20] while the **1**-based devices are the most stable in this series. Quite likely, the device degradation is related to the irreversible oxidation degradation toward Cu(II) species upon device driving and the over oxidation rates depending on the applied voltages, as suggested by the electrochemical and EIS characterizations—vide supra. Hence, we decided to decouple hole injection/transport and exciton formation using the multilayered LEC with the architecture ITO/PEDOT:PSS/CBP(10–15 nm)/Cu-iTMC(85 nm)/Al (CBP is 4,4′-Bis(9-carbazolyl)-1,1′-biphenyl).[19,20]

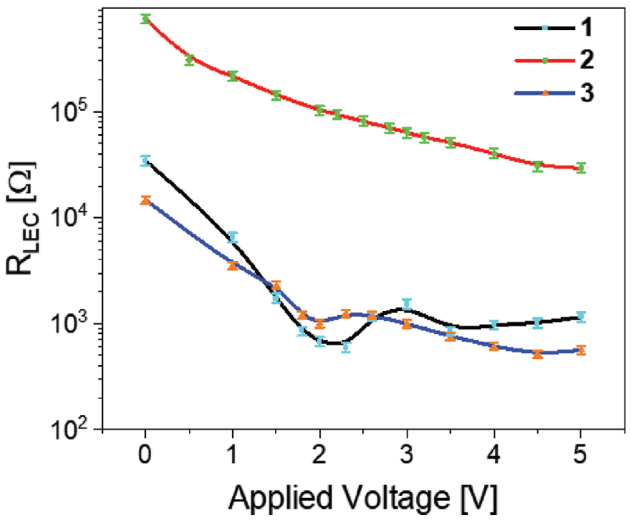

Figure 6. Resistance profile at different voltages in EIS assays conducted at 0–5 V for **1–3** LEC devices. Every measured point is reported with its corresponding error bar.

These devices were driven at 5 mA to allow a straightforward comparison between performances of single- and multilayered devices (Table 3; Figure 7 and Figure S8, Supporting Information). In detail, multilayered LECs showed enhanced irradiances (Table 3, e.g., ≈155 µW cm^{-2} vs 90 µW cm^{-2} for CBP/**1** and **1**, respectively), as well as enhanced stabilities (Table 3, e.g., 0.6 h/91 J vs 0.13 h/12 J for CBP/**1** and **1**, respectively). This represents almost an order of magnitude of improvement for all the figures-of-merit without affecting device chromaticity (Table 3). Indeed, the electroluminescence band is the same for single- and multilayered devices regardless of the type of copper(I) complex (Figure S8, Supporting Information). This indicates that hole injection occurs in the CBP layer, and then it is transferred to the Cu-iTMC, while electron injection and accumulation is effective in the Cu-iTMC emitting layer. As such, the formation of oxidized Cu-iTMC species is significantly reduced, leading to enhanced stabilities and efficiencies.[18,19]

Since **1** featured the best performance among the series (Table 3), we further fabricated host–guest white-emitting LECs using **1** as guest along with a blue-emitting host material.

Table 3. Figures-of-merit of devices based on **1**–**3**.

Active layer	Irr_{max}[a)] [μW cm^{-2}]	t_{on}[b)] [h]	$t_{1/2}$[c)] [h]	Efficiency [lm W^{-1}]	EQE [%]	E_{tot}[d)] [mJ]	λ_{max} (x/y CIE) [nm]
1	89.9	0.028	0.13	0.08	0.032	11.96	631(0.59/0.41)
CBP/**1**	152.8	0.19	0.57	0.12	0.048	90.72	626 (0.58/0.41)
2	57.05	0.013	0.09	0.04	0.016	5.10	661(0.66/0.31)
CBP/**2**	74.4	0.071	0.35	0.06	0.024	26.4	649 (0.65/0.32)
3	67.9	0.010	0.067	0.05	0.021	4.62	624 (0.59/0.41)
CBP/**3**	93.3	0.022	0.42	0.06	0.026	39.72	624 (0.58/0.41)
CBP:**1**	–	0.014	0.084	–	0.003	1.28	393, 478, 639 (0.31/0.32)

[a)]Maximum irradiance achieved throughout the measurement; [b)]Time to reach the maximum luminance; [c)]Time at which the maximum luminance halves its value; [d)]Total emitted energy of the device calculated by integrating the radiant flux from $t = 0$ to $t = 1/5$ (where the maximum luminance reaches one-fifth of its value).

Following our previous reports, the CBP is an optimal candidate for the host role, as it features a bluish electroluminescence response that fit to the MLCT absorption band of **1** (Figure S9, Supporting Information).[18,19] The device architecture ITO/PEDOT:PSS/CBP:1/Al was optimized with a mass ratio CBP:**1** of 98:2 in terms of white color emission. In short, the electroluminescence response consists of a broad emission with balanced peaks at 400/500, and 650 nm that correspond to the CBP and **1**, respectively (**Figure 8**). This is associated with x/y CIE color coordinates of 0.31/0.32 and CRI of 90 that are stable over the device lifespan (Table 3). Finally, these white LECs exhibited a moderate luminance of 12 cd m^{-2} at 15 mA pulsed current. This represents an improvement in comparison with previous reports, in which CBP:Cu-iTMC host–guest white LECs could only reach luminances of 5 cd m^{-2} at pulsed 25 mA.[20]

3. Conclusion

We demonstrate the successful design of a series of red-emitting copper(I) complexes with the S-bridged bis-pyrimidinyl N^N ligand replacing the pyridine part by i) pyrazine, ii) π-expanded quinoxaline, and iii) electron-deficient pyrimidinyl moieties. This design led the lowest energy emitting complexes in this family of Cu-iTMCs, featuring, in addition, high PLQYs and a TADF emission mechanism. This resulted in well-performing single- and multilayered red-emitting LECs, reaching irradiances of 150 μW cm^{-2}, EQE of 0.05%, and stabilities of 90 mJ.

This was further exploited to fabricate host:guest white LECs combining CBP and the best Cu-iTMC, **1**. Devices with luminances of 12 cd m^{-2} in concert with excellent white quality (CRI = 90) stable over the lifespan stand out the state-of-the-art in white Cu-iTMC LECs. In view of all of the aforementioned, this work provides important molecular design guidelines on the preparation of low-energy-emitting Cu-iTMCs for application in both, red- and white-emitting lighting technologies.

4. Experimental Section

Synthesis and Characterization: All commercial compounds were used as received, unless stated otherwise. All reactions were carried out using standard Schlenk techniques. All air- and water-sensitive reactions were carried out under dry argon atmosphere. Solvents were purchased from Carlo Erba, when required they were distilled and then degassed prior to their use by bubbling argon gas directly in the solvent. NMR spectra were recorded at room temperature on 500 MHz and 600 MHz Bruker spectrometers at 298 K unless stated otherwise. Proton (^{1}H) NMR information was given in the following format: multiplicity (s, singlet; d, doublet; t, triplet; q, quartet; qui, quintet; sex, sextet; sept, septet; m, multiplet), coupling constant(s) (*J*) in Hertz (Hz), number of protons. The prefix app was occasionally applied when the true signal multiplicity was unresolved and br indicated the signal in question was broadened. Carbon (^{13}C) NMR spectra were reported in ppm (δ) relative to residual

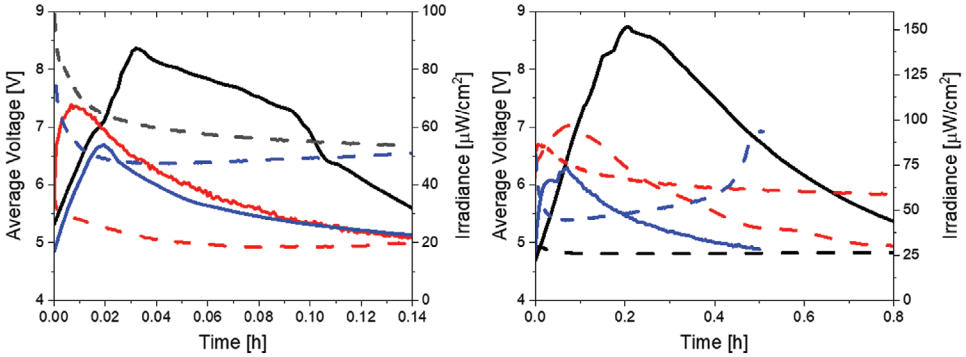

Figure 7. Average voltage (dashed lines) and irradiance (solid lines) versus time of single- (left) and multilayered (right) **1** (black), **2** (blue), and **3** (red) LECs driven at pulsed 5 mA.

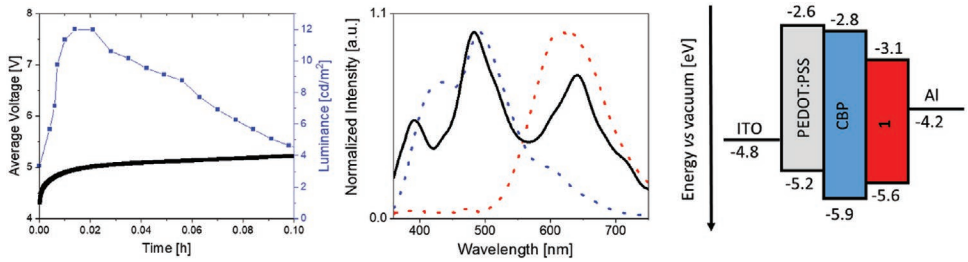

Figure 8. Average voltage and luminance versus time (left) of CBP:**1**-LECs driven at pulsed 15 mA. The electroluminescence spectrum (right) of the CBP:**1** (black solid line), CBP (blue dashed line), and 1 (red dashed line) LECs driven at pulsed 5 mA.

$CHCl_3$ (δ77.0) unless stated otherwise idem for phosphor (^{31}P) and fluor (^{18}F) NMR. HRMS were performed by LCMT analytical services.

Pyrazine-2-thiol[34]: To a solution of 2-chloropyrazine (1.00 g, 8.73 mmol, 1 equiv.) in distilled dimethylformamide (DMF, 1 M) was added $NaSH{\cdot}H_2O$ (90%) (1.55 equiv). After 2 h at 60 °C, the mixture was cooled down to 0 °C. The resulting precipitate (NaCl) was filtered and washed with DMF (5 mL). From filtrate, compound **1** was obtained by precipitation from diethyl ether (250 mL) affording a yellow solid (647 mg, 5.77 mmol, 66%). ^1H NMR (500 MHz, DMSO-d_6, δ): 8.05 (s, 1H), 7.69 (d, J = 2.6 Hz, 1H), 7.43 (t, J = 2.3 Hz, 1H) ppm, SH not found, in good agreement with the literature.[34]

General Procedure for the Preparation of Di(pyrazin-2-yl)sulfane and 2-(pyrazin-2-ylthio)quinoxaline: To a solution of K_2CO_3 (2 equivalents) in dry acetonitrile (0.5 M) was added the thiol derivative (1 equivalent) followed by the addition of the halide derivative (1.2 equivalents). After 16 h at 84 °C, the reaction mixture was cooled down to rt, filtered through Celite, concentrated *in vacuo*, then purified by flash column chromatography.

Di(pyrazin-2-yl)sulfane: Prepared following the general procedure from pyrazine-2-thiol (229 mg, 2.00 mmol) and 2-iodopyrazine (237 µL, 2.40 mmol). Purification by flash column chromatography (pentane/ethyl acetate: 7/3, R_f: 0.3) afforded a white solid (225 mg, 1.18 mmol, 59%). ^1H NMR: (500 MHz, $CDCl_3$) δ_H: 8.72 (s, 2H), 8.48 (d, J = 2.5 Hz, 2H), 8.46 (d, J = 2.5 Hz, 2H) ppm. ^{13}C NMR: (126 MHz, $CDCl_3$) δ_C: 152.9 (C_q), 146.9 (CH), 144.9 (CH), 142.8 (CH) ppm. In good agreement with the literature.[54]

2-(Pyrazin-2-ylthio)quinoxaline: Prepared following the general procedure from pyrazine-2-thiol (300 mg, 2.67 mmol) and 2-chloroquinoxaline (528 mg, 3.21 mmol). Purification by flash column chromatography afforded a brown solid (513 mg, 2.14 mmol, 80%). ^1H NMR (600 MHz, $CDCl_3$) δ_H: 8.87 (s, 1H), 8.81 (s, 1H), 8.48 (s, 2H), 8.09–8.02 (m, 1H), 7.96–7.89 (m, 1H), 7.75–7.68 (m, 2H) ppm. ^{13}C NMR: (151 MHz, $CDCl_3$) δ_C: 152.5 (C_q), 152.1 (C_q), 147.3 (CH), 146.0 (CH), 144.9 (CH), 142.9 (CH), 142.6 (C_q), 140.8 (C_q), 130.8 (CH), 130.0 (CH), 129.3 (CH), 128.8 (CH) ppm. HRMS (ESI): m/z Calcd for: $C_{12}H_8N_2S$, 241.0548 $[M+H]^+$, found: 241.0560.

2-(Pyrazin-2-ylthio)-4-(trifluoromethyl)pyrimidine: Prepared following an SNAr procedure as reported in the literature.[36] To a solution of KOH (2 equiv) in dry DMSO (0.5 M) under argon atmosphere was added pyrazin-2-thiol (224 mg, 2.00 mmol, 1 equiv) followed by the addition of 2-chloro-4-(trifluoromethyl)pyrimidine (290 µL, 2.40 mmol, 1.2 equiv). After 4 h at 140 °C, the reaction was cooled down to rt, a saturated solution of KCl (100 mL) was added, the organic layer was extracted with CH_2Cl_2 (3 × 100 mL), combined, washed with a saturated solution of KCl (300 mL), filtered, and concentrated *in vacuo*. Purification by flash column chromatography afforded a brown oil (333 mg, 1.29 mmol, 64%). ^1H NMR: (600 MHz, $CDCl_3$) δ_H: 8.97 (s, 1H), 8.75 (d, J = 5.0 Hz, 1H), 8.64 (t, J = 2.0 Hz, 1H), 8.64 (t, J = 2.0 Hz, 1H), 7.37 (d, J = 5.0 Hz, 1H) ppm. ^{13}C NMR: (151 MHz, $CDCl_3$) δ_C: 172.1 (d, J = 0.5 Hz, C_q), 160.1 (CH), 156.4 (q, J = 37.0 Hz, C_q), 150.5 (CH), 150.1 (C_q), 145.1 (CH), 144.0 (CH), 120.0 (q, J = 275.5 Hz, C_q), 113.5 (q, J = 2.6 Hz, CH) ppm. ^{19}F NMR: (471 MHz, $CDCl_3$) δ_F: –70.20 ppm.

*General Procedure for Complexes **1–3***: A solution of $[Cu(CH_3CN)_4][PF_6]$ (1 equiv) and DPEphos (1 equiv) in dry and degassed CH_2Cl_2 (0.01 M) under argon was stirred for 1 h at room temperature, then N∧N ligand (1 equiv) was added. The mixture was then filtered through Celite, concentrated in vacuo. The residue was dissolved in a minimum of CH_2Cl_2 then precipitated by the addition of pentane and ether. The precipitate was washed by pentane and ether. The pure product was afforded by recrystallization in acetone/methylene chloride/diethyl ether/pentane.

*Copper(I) [2-(2-diphenylphosphanylphenoxy)phenyl]-diphenylphosphane, di(pyrazin-2-yl)sulfane] hexafluorophosphate Complex **1***: Following the general procedure from 0.49 mmol, Yield: 420 mg, 0.45 mmol, 91%. ^1H NMR: (600 MHz, CD_2Cl_2) δ_H: 8.99 (d, J = 1.5 Hz, 2H), 8.25 (d, J = 2.8 Hz, 2H), 7.85 (dd, J = 2.8, 1.5 Hz, 2H), 7.36 (t, J = 7.8 Hz, 4H), 7.32 (dt, J = 7.8, 1.6 Hz, 2H), 7.23 (t, J = 7.7 Hz, 8H), 7.18–7.14 (m, 8H), 7.06–7.00 (m, 4H), 6.82 (ddt, J = 8.0, 4.2, 1.6 Hz, 2H). ^{13}C NMR: (151 MHz, CD_2Cl_2) δ_C: 158.0 (t, J = 5.9 Hz, 2 C_q), 150.0 (2 CH), 148.9 (2 C_q), 146.1 (2 CH), 145.1 (2 CH), 134.8 (t, J = 1.1 Hz, 2 CH), 133.9 (t, J = 9.0 Hz, 8 CH), 133.1 (2 CH), 131.2 (4 CH), 130.2 (t, J = 18.3 Hz, 4 Cq), 129.6 (d, J = 6.5 Hz, 8 CH), 126.0 (t, J = 4.8 Hz, 2 CH), 123.7 (t, J = 17.4 Hz, 2 C_q), 120.9 (2 CH) ppm. ^{31}P NMR: (243 MHz, CD_2Cl_2) δ_P: –11.71 (br s, 2P), –144.58 (hept, J = 713.4 Hz, PF_6) ppm. ^{19}F NMR: (565 MHz, CD_2Cl_2) δ_F: –73.49 (d, J = 710.7 Hz, PF_6). HRMS (ESI) m/z: $[M - PF_6]^+$ calcd for $C_{44}H_{34}CuN_4OP_2S$, 791.1225; found, 791.1224.

*Copper(I) [2-(2-diphenylphosphanylphenoxy)phenyl]-diphenylphosphane, 2-(pyrazin-2-ylthio)quinoxaline] hexafluorophosphate Complex **2***: Following the general procedure described for complexes. Using 0.95 mmol, Yield: 930 mg, 0.94 mmol, 99%. ^1H NMR: (500 MHz, acetone-d_6) δ_H 8.96 (s, 2H), 8.59 (s, 1H), 8.50 (s, 1H), 8.09 (d, J = 8.4 Hz, 1H), 7.82 (d, J = 8.4 Hz, 1H), 7.78 (t, J = 7.6 Hz, 1H), 7.53 (t, J = 7.6 Hz, 1H), 7.43–7.40 (m, 6H), 7.34–7.30 (m, 16H), 7.12 (d, J = 8.2 Hz, 2H), 7.09 (t, J = 7.6 Hz, 2H), 6.79 (d, J = 7.6, 2H) ppm. ^{13}C NMR: (125 MHz, acetone-d_6) δ_C 158.5 (t, J = 5.7 Hz, 2 C_q), 152.5 (C_q), 152.4 (C_q), 149.2 (CH), 147.7 (CH), 146.7 (CH), 145.0 (CH), 142.6 (C_q), 142.2 (C_q), 135.1 (2 CH), 134.5 (t, J = 8.0 Hz 8C, CH), 133.5 (4 CH), 132.0 (CH), 131.7 (CH), 131.6 (2 CH), 131.1 (t, J = 18.1 Hz, 4 C_q), 130.3 (CH), 130.1 (t, J = 4.9 Hz, 8 CH), 129.1 (CH), 126.2 (t, J = 2.5 Hz, 2 CH), 124.3 (t, J = 15.9 Hz, 2 C_q), 121.2 (2 CH) ppm. ^{31}P NMR: (243 MHz, acetone-d_6) δ_P: –15.43 (br s, 2P), –144.25 (hept, J = 709.9 Hz, PF_6) ppm. ^{19}F NMR: (565 MHz, acetone-d_6) δ_F: –72.57 (d, J = 708.3 Hz, PF_6) ppm. HRMS (ESI) m/z: $[M - PF_6]^+$ calcd for $C_{48}H_{36}CuN_4OP_2S$, 841.1381; found, 841.1391.

*Copper(I) [2-(2-diphenylphosphanylphenoxy)phenyl]-diphenylphosphane, 2-(pyrazin-2-ylthio)-4-(trifluoromethyl)pyrimidine] hexafluorophosphate Complex **3***: Following the general procedure described for complexes. Using 0.50 mmol, Yield: 431.4 mg, 0.43 mmol, 86%. ^1H NMR: ^1H NMR (500 MHz, CD_2Cl_2) δ_H (500 MHz, CD_2Cl_2, δ): 8.59 (s, 1H), 8.13–8.08 (m, 2H), 7.40–7.28 (m, 15H), 7.24–7.20 (m, 8H), 7.14 (d, J = 5.4 Hz, 1H), 7.05–6.99 (m, 4H), 6.81–6.77 (m, 2H). ^{13}C NMR (CD_2Cl_2, 151 MHz): δ 169.3–168.1 (m, C_q), 160.6 (CH), 158.0 (2 C_q), 156.7 (q, J = 37.8 Hz, C_q), 150.4 (CH), 148.6 (C_q), 147.0–145.5 (m, C_q), 134.8 (2 CH), 134.0 (t, J = 7.6 Hz, 8 CH), 133.1 (4 CH), 131.3 (2 CH), 130.5–129.4 (m, 9 carbons overlapped, 8 from DPEPhos + 1 from N∧N ligand), 126.0 (2 CH), 123.4 (t, J = 15.6 Hz, 2 CH), 120.7 (2 CH), 120.0 (q, J = 277.8 Hz, C_q), 116.8 (CH) ppm. ^{31}P NMR (243 MHz, CD_2Cl_2, δ): –12.4 (br s, 2P), –144.7 (sept, J = 712.9 Hz, PF_6). ^{19}F NMR (565 MHz, CD_2Cl_2, δ): –70.2 (CF_3), –73.1 (d, J = 711.7 Hz, PF_6). IR (neat) ν = 3061.4, 3013.2, 2970, 1739, 1565,

1479, 1461, 1435, 1349, 1332, 1260, 1216, 1161, 1122, 1097, 1072, 999, 875, 835 cm^{-1}. HRMS (ESI) *m/z*: $[M - PF_6]^+$ calcd for $C_{45}H_{33}CuF_3N_3OP_2S$, 859.1088; found, 859.1098.

XRD Analysis: [CCDC 2109488 (for **1**) and 2109489 (for **2**) contain the supplementary crystallographic data for this paper. These data can be obtained free of charge from The Cambridge Crystallographic Data Centre via www.ccdc.cam.ac.uk/data_request/cif.]

Fabrication and Characterization of Thin Films: A Shimatzu 2700-I UV-Vis spectrometer was used to acquire UV-VIS spectral data, and an FS5 Spectrofluorometer with integrating sphere (Edinburgh Instruments) to acquire photoluminescence spectra and PLQYs. Average excited states lifetimes $<\tau>$ were measured with an Edinburgh TCSPC Instrument by using a microsecond lamp (λ_{exc} = 330 nm, 100 Hz frequency) as excitation source.

Then, the average lifetime was calculated with the following formula: $R\ (t) = \sum_{2}^{i=1} A_i e^{-t/\tau_i}$

In case of a double component decay, it equals to $\langle\tau\rangle = \frac{A_1\tau_1^2 + A_2\tau_2^2}{A_1\tau_1 + A_2\tau_2}$, where A_1 and A_2 are relative amplitudes for τ_1 and τ_2, respectively.

The morphology of the devices was measured via AFM with a Park XE150 instrument (Park Systems Corp., Suwon, South Korea).

Electrochemical Characterization in Solution: The CV was carried out with an Autolab PGSTAT204 potentiostat (Metrohm GmbH) driven by the Nova 2.1 software. The working electrode comprised a thin film of the material-under-study coated on an Au-covered glass substrate, a Pt rod was the counter electrode, a Ag wire was the quasi-reference electrode, and 0.1 M $THABF_4$ (Sigma- Aldrich) in anhydrous CH_3CN was the electrolyte. All CV potentials were reported versus the ferrocene/ferrocenium ion (Fc/Fc^+) reference potential. The reduction/oxidation onset potentials were defined as the intersection of the baseline with the tangent of the current at the half-peak-height. The energy structure (i.e., the HOMO and LUMO levels) of the material-under-study was derived using the equation E_{vacuum} level = $-e\cdot(5.1\ V + V_{Fc/Fc^+})$.

Device Preparation and Characterization: Commercial ITO substrates (Naranjo Substrates) were cleaned in a four-steps procedure involving detergent, water, ethanol, and isopropanol under ultrasonication for 15 min each. Then, they were subjected to 8 min UV-ozone cleaning. Afterward, a PEDOT:PSS (Clevios Ai 4083) layer (70 nm) was spin-coated on top of the clean substrates. The PEDOT:PSS was mixed with isopropanol in a volumetric ratio of 3:1, and spin-coated onto the plates at 1900 rpm for 60 s. An annealing step followed (1 h, 120 °C). The Cu-iTMCs were spin-coated on top of the PEDOT:PSS layer from a 12 mg mL^{-1} butanone solution to achieve 80 nm thick layers, as obtained via profilometry assays with an AlphaStep 500 profilometer (KLA Tencor). In the case of multilayered devices, a layer of CBP in tetrahydrofuran (THF, 5 mg mL^{-1}) was first deposited onto the PEDOT:PSS layer by rotation at 3000 rpm for a minute. The thickness of the layer was of 15 nm. Then, the Cu-iTMC layer was deposited as previously described. To obtain white-emitting devices, a mixture of the CBP and Cu-iTMC in a ratio of 98:2 (weight/weight) was solubilized in THF in a concentration of 5 mg mL^{-1} and spin-coated onto the PEDOT:PSS layer at 800 rpm for 1 min to yield 60 nm thick layers. All the devices were then dried under vacuum for 2 h before being inserted in a glovebox (<0.1 ppm O_2 and H_2O, Angstrom Engineering). Finally, 90 nm thick aluminum cathodes were evaporated under physical vapor deposition in a high vacuum Angstrom Covap evaporator. The device active area was of 10 mm^2. The so-fabricated LECs were measured with an Avantes spectrophotometer (Avaspec-ULS2048L-USB2) with a calibrated integrated sphere Avasphere 30-Irrad and a Botest OLT OLED Lifetime-Test System, as described in previous contributions.[19,55] EIS assays were performed with a potentiostat/galvanostat PGSTAT204 (Metrohm μAutolabIII) with EIS frequency response analyzer module (FRA2). The applied voltage ranged from 0 to 5 V. The obtained data were fitted with the Nova software 1.1 using the circuit model shown in Figure S7 in the Supporting Information, as described in previous contributions.[19,20]

Supporting Information

Supporting Information is available from the Wiley Online Library or from the author.

Acknowledgements

This work was supported by the Ministère de la Recherche et des Nouvelles Technologies, CNRS (Centre National de la Recherche Scientifique), and the LABEX SynOrg (ANR-11-LABX-0029). S.G. acknowledges the Graduate School of Research XL-Chem (ANR-18-EURE-0020 XL-Chem) and the Région Normandie for financial support.. R.D.C. acknowledges the European Union's Horizon 2020 research and innovation FET-OPEN under grant agreement ARTIBLED No 863170, the ERC-Co InOutBioLight No. 816856, and the MSCA-ITN STiBNite No. 956923.

Open access funding enabled and organized by Projekt DEAL.

Conflict of Interest

The authors declare no conflict of interest.

Data Availability Statement

Research data are not shared.

Keywords

copper(I) complexes, deep-red emission, electroluminescence, light-emitting electrochemical cells, white-emitting sources

Received: September 17, 2021
Revised: October 21, 2021
Published online: November 23, 2021

[1] M. S. Shur, A. Žukauskas, *Proc. IEEE* **2005**, *93*, 1691.
[2] C. J. Humphreys, *Solid-State Lighting* **2019**, *33*, 459.
[3] S. Tang, L. Edman, *Top. Curr. Chem.* **2016**, *374*, 40.
[4] G. Hernandez-Sosa, A. J. Morfa, N. Jürgensen, S. Tekoglu, J. Zimmermann, in *Light-Emitting Electrochemical Cells: Concepts, Advances and Challenges*, (Ed: R. D. Costa), Springer International Publishing, Basel **2017**, pp. 139–163.
[5] S. van Reenen, M. Kemerink, in *Light-Emitting Electrochemical Cells: Concepts, Advances and Challenges*, (Ed: R. D. Costa), Springer International Publishing, Basel **2017**, pp. 3–45.
[6] R. D. Costa, *Light-Emitting Electrochemical Cells: Concepts, Advances and Challenges*, Springer International Publishing, Basel **2017**.
[7] S. B. Meier, S. Van Reenen, B. Lefevre, D. Hartmann, H. J. Bolink, A. Winnacker, W. Sarfert, M. Kemerink, *Adv. Funct. Mater.* **2013**, *23*, 3531.
[8] S. Van Reenen, R. A. J. Janssen, M. Kemerink, *Adv. Funct. Mater.* **2012**, *22*, 4547.
[9] J. C. deMello, *Phys. Rev. B* **2002**, *66*, 235210.
[10] J. M. Carbonell-Vilar, E. Fresta, D. Armentano, R. D. Costa, M. Viciano-Chumillas, J. Cano, *Dalton Trans.* **2019**, *48*, 9765.
[11] E. Fresta, R. D. Costa, *J. Mater. Chem. C* **2017**, *5*, 5643.
[12] Z. Yu, L. Li, H. Gao, Q. Pei, *Sci. China: Chem.* **2013**, *56*, 1075.
[13] E. Fresta, J. Dosso, J. Cabanillas-Gonzalez, D. Bonifazi, R. D. Costa, *Adv. Funct. Mater.* **2020**, *30*, 1906830.

[14] S. Kanagaraj, A. Puthanveedu, Y. Choe, *Adv. Funct. Mater.* **2020**, *30*, 1907126.
[15] E. Fresta, A. Charisiadis, L. M. Cavinato, N. Palandjian, K. Karikis, N. Vasilis, G. Charalambidis, A. G. Coutsolelos, R. D. Costa, *Adv. Photonics Res.* **2021**, *2*, 2000188.
[16] A. F. Henwood, E. Zysman-Colman, *Top. Curr. Chem.* **2016**, *374*, 36.
[17] G. U. Mahoro, E. Fresta, M. Elie, D. Nasso, Q. Zhang, J. Lohier, J. Renaud, M. Linares, R. Wannemacher, J. Cabanillas-Gonzalez, R. D. Costa, S. Gaillard, *Dalton Trans.* **2021**, *50*, 11049.
[18] M. D. Weber, E. Fresta, M. Elie, M. E. Miehlich, J.-L. Renaud, K. Meyer, S. Gaillard, R. D. Costa, *Adv. Funct. Mater.* **2018**, *28*, 1707423.
[19] E. Fresta, G. Volpi, M. Milanesio, C. Garino, C. Barolo, R. D. Costa, *Inorg. Chem.* **2018**, *57*, 10469.
[20] E. Fresta, M. D. Weber, J. Fernandez-Cestau, R. D. Costa, *Adv. Opt. Mater.* **2019**, *7*, 1900830.
[21] R. D. Costa, D. Tordera, E. Ortí, H. J. Bolink, J. Schönle, S. Graber, C. E. Housecroft, E. C. Constable, J. A. Zampese, *J. Mater. Chem.* **2011**, *21*, 16108.
[22] S. Keller, A. Pertegás, G. Longo, L. Martínez, J. Cerdá, J. M. Junquera-Hernández, A. Prescimone, E. C. Constable, C. E. Housecroft, E. Ortí, H. J. Bolink, *J. Mater. Chem. C* **2016**, *4*, 3857.
[23] M. Alkan-Zambada, S. Keller, L. Martínez-Sarti, A. Prescimone, J. M. Junquera-Hernández, E. C. Constable, H. J. Bolink, M. Sessolo, E. Ortí, C. E. Housecroft, *J. Mater. Chem. C* **2018**, *6*, 8460.
[24] S. Keller, F. Brunner, J. M. Junquera-Hernández, A. Pertegás, M.-G. La-Placa, A. Prescimone, E. C. Constable, H. J. Bolink, E. Ortí, C. E. Housecroft, *ChemPlusChem* **2018**, *83*, 217.
[25] S. Keller, E. C. Constable, C. E. Housecroft, M. Neuburger, A. Prescimone, G. Longo, A. Pertegás, M. Sessolo, H. J. Bolink, *Dalton Trans.* **2014**, *43*, 16593.
[26] N. Arnosti, F. Brunner, I. Susic, S. Keller, J. M. Junquera-Hernández, A. Prescimone, H. J. Bolink, M. Sessolo, E. Ortí, C. E. Housecroft, E. C. Constable, *Adv. Opt. Mater.* **2020**, *8*, 1901689.
[27] F. Brunner, L. Martínez-Sarti, S. Keller, A. Pertegás, A. Prescimone, E. C. Constable, H. J. Bolink, C. E. Housecroft, *Dalton Trans.* **2016**, *45*, 15180.
[28] M. Elie, F. Sguerra, F. Di Meo, M. D. Weber, R. Marion, A. Grimault, J.-F. Lohier, A. Stallivieri, A. Brosseau, R. B. Pansu, J.-L. Renaud, M. Linares, M. Hamel, R. D. Costa, S. Gaillard, *ACS Appl. Mater. Interfaces* **2016**, *8*, 14678.
[29] M. Elie, S. Gaillard, J. L. Renaud, in *Light-Emitting Electrochemical Cells: Concepts, Advances and Challenges*, (Ed: R. D. Costa), Springer International Publishing, Basel **2017**, pp. 287–327.
[30] E. Fresta, R. D. Costa, *Adv. Funct. Mater.* **2020**, *30*, 1908176.
[31] H. Su, Y. Chen, K. Wong, *Adv. Funct. Mater.* **2019**, *30*, 1906898.
[32] M. Elie, M. D. Weber, F. Di Meo, F. Sguerra, J.-F. Lohier, R. B. Pansu, J.-L. Renaud, M. Hamel, M. Linares, R. D. Costa, S. Gaillard, *Chem. – Eur. J.* **2017**, *23*, 16328.
[33] C. M. Brown, C. Li, V. Carta, W. Li, Z. Xu, P. H. F. Stroppa, I. D. W. Samuel, E. Zysman-Colman, M. O. Wolf, *Inorg. Chem.* **2019**, *58*, 7156.
[34] J. W. Lee, B. Lee, N. D. Kim, *Arch. Pharm. Res.* **2001**, *24*, 16.
[35] F. Yan, H. Liang, J. Song, J. Cui, Q. Liu, S. Liu, P. Wang, Y. Dong, H. Liu, *Org. Lett.* **2017**, *19*, 86.
[36] Y. Yuan, I. Thomé, S. H. Kim, D. Chen, A. Beyer, J. Bonnamour, E. Zuidema, S. Chang, C. Bolm, *Adv. Synth. Catal.* **2010**, *352*, 2892.
[37] D. G. Cuttell, S.-M. Kuang, P. E. Fanwick, D. R. McMillin, R. A. Walton, *J. Am. Chem. Soc.* **2002**, *124*, 6.
[38] L. Yang, D. R. Powell, R. P. Houser, *Dalton Trans.* **2007**, 955.
[39] N. Armaroli, G. Accorsi, F. Cardinali, A. Listorti, *Photochemistry and Photophysics of Coordination Compounds: Copper*, Springer, Berlin, Heidelberg **2007**.
[40] R. Czerwieniec, M. J. Leitl, H. H. H. Homeier, H. Yersin, *Coord. Chem. Rev.* **2016**, *325*, 2.
[41] E. Fresta, G. Volpi, C. Garino, C. Barolo, R. D. Costa, *Polyhedron* **2018**, *140*, 129.
[42] M. J. Leitl, D. M. Zink, A. Schinabeck, T. Baumann, D. Volz, H. Yersin, *Top. Curr. Chem.* **2016**, *374*, 25.
[43] M. J. Leitl, V. A. Krylova, P. I. Djurovich, M. E. Thompson, H. Yersin, *J. Am. Chem. Soc.* **2014**, *136*, 16032.
[44] R. Czerwieniec, H. Yersin, *Inorg. Chem.* **2015**, *54*, 4322.
[45] N. Notsuka, H. Nakanotani, H. Noda, K. Goushi, C. Adachi, *J. Phys. Chem. Lett.* **2020**, *11*, 562.
[46] H. Tanaka, K. Shizu, J. Lee, C. Adachi, *J. Phys. Chem. C* **2015**, *119*, 2948.
[47] I. Andrés-Tomé, J. Fyson, F. Baiao Dias, A. P. Monkman, G. Iacobellis, P. Coppo, *Dalton Trans.* **2012**, *41*, 8669.
[48] O. Moudam, A. Kaeser, B. Delavaux-Nicot, C. Duhayon, M. Holler, G. Accorsi, N. Armaroli, I. Séguy, J. Navarro, P. Destruel, J. F. Nierengarten, *Chem. Commun.* **2007**, *3092*, 3077.
[49] C. M. Cardona, W. Li, A. E. Kaifer, D. Stockdale, G. C. Bazan, *Adv. Mater.* **2011**, *23*, 2367.
[50] B. M. D. Puscher, M. F. Aygüler, P. Docampo, R. D. Costa, *Adv. Energy Mater.* **2017**, *7*, 1602283.
[51] E. Fresta, K. Baumgärtner, J. Cabanillas-Gonzalez, M. Mastalerz, R. D. Costa, *Nanoscale Horiz.* **2020**, *5*, 473.
[52] A. Pertegás, D. Tordera, J. Serrano-Pérez, E. Ortí, J. B. Henk, *J. Am. Chem. Soc.* **2013**, *135*, 18008.
[53] S. Tang, H. A. Buchholz, L. Edman, *J. Mater. Chem. C* **2015**, *3*, 8114.
[54] K. H. V. Reddy, V. P. Reddy, J. Shankar, B. Madhav, B. S. P. Anil Kumar, Y. V. D. Nageswar, *Tetrahedron Lett.* **2011**, *52*, 2679.
[55] E. Fresta, J. Dosso, J. Cabanillas-Gonzalez, D. Bonifazi, R. D. Costa, *ACS Appl. Mater. Interfaces* **2020**, *12*, 28426.